Fuel 211 (2018) 331–340

Contents lists available at ScienceDirect

Fuel

journal homepage: www.elsevier.com/locate/fuel

Full Length Article

Design and demonstration of a prototype 1.5 kW_{th} hybrid solar/autothermal steam gasifier

Alexander P. Muroyama[a], Iacopo Guscetti[b], Garrett L. Schieber[a], Sophia Haussener[b], Peter G. Loutzenhiser[a,*]

[a] George W. Woodruff School of Mechanical Engineering, Georgia Institute of Technology, Atlanta, GA 30332-0405, USA
[b] Institute of Mechanical Engineering, École Polytechnique Fédérale de Lausanne, 1015 Lausanne, Switzerland

ARTICLE INFO

Keywords:
Solar gasification
Synthesis gas
Autothermal gasification
Fluidized bed

ABSTRACT

A 1.5 kW_{th} hybrid solar/autothermal steam gasifier was designed and tested for continuously producing synthesis gas. Time-averaged responses to a series of inlet flow conditions were examined in a high-flux solar simulator. The gasifier consisted of a SiC absorbing/emitting tube inside of a windowless Al_2O_3-SiC cavity containing a fluidized bed indirectly irradiated by concentrated irradiation. Monte Carlo ray-tracing was performed to examine heat flux distributions and determine optimal prototype geometry and lamp settings. An experimental design with replicates was used to examine the effects of H_2O:C, O_2:C, and feedstock with two-way analyses of variance. Carbon conversions of up to 0.79 were achieved, and maximum cold gas ratio and solar-to-fuel efficiency were 1.16 and 22%, respectively. Introduction of O_2 led to a significant increase in bed temperature. Higher performance was observed using activated charcoal compared with lignite coal. The gasifier results indicate that a hybrid solar/autothermal gasification process may be used to overcome disturbances due to solar transients.

1. Introduction

Utilizing concentrated solar irradiation to drive thermochemical processes affords a wide range of paths for producing sustainable fuels. Previous work has examined the concept of coupling together autothermal and solar-driven gasification processes within a single gasifier, allowing for continuous, 24-h production of H_2- and CO-rich synthesis gas (syngas) for downstream fuel or chemical synthesis [1–4]. Fischer-Tropsch (F-T) synthesis allows for the production of drop-in liquid hydrocarbons for the transportation sector. Three modes of operation were realized: (1) solar-driven allothermal gasification during periods with abundant sunlight; (2) autothermal gasification at night or during cloudy periods with the sun obscured; and (3) combined gasification during periods of low to moderate sunlight. Kinetic analyses for the relevant combustion and gasification reactions were performed with activated charcoal, bituminous coal char, and *miscanthus x giganteus* char as the carbonaceous feedstocks [2].

Solar-driven allothermal gasifiers transfer heat to the reactants using two different configurations: (1) directly and (2) indirectly irradiated [5]. Indirectly-irradiated gasifiers avoid use of a quartz glass window, which is prone to fouling at the expense of irreversibilities resulting from conducting heat through an opaque absorber [6]. Previous indirectly-irradiated designs have implemented absorbing/emitting tubes [7–12], plates [13–15], or cylindrical cavities [16,17] to transfer heat to reactants. SiC is commonly used as an absorbing material due to its favorable properties: high emissivity, high thermal conductivity, inertness at high temperatures, and low coefficient of thermal expansion.

Prominent solar-driven gasifier designs that have been examined in literature have employed entrained flow [11,16,18], drop tubes [7,8,10], packed beds [15,19,20], and fluidized beds [12,21–28]. Entrained-flow and drop-tube gasifiers generally have very short residence times while benefiting from enhanced heat and mass transfer. A few studies have been able to achieve high carbon conversions despite these limitations [7,16,18]. Packed beds are able to handle a wide variety of feedstocks and particle sizes with long residence times, but face challenges with heat and mass transport. In addition, all previous packed-bed investigations have operated in a batch-mode. An additional design has explored the use of molten salt as a reaction and heat transfer medium for gasification [17,29,30].

Fluidized beds are used in combustion and gasification applications, as they allow for continuous operation, rapid adjustment of the reactant inputs, high particle residence times, and high gas-solid contact with efficient heat and mass transport. Directly-irradiated fluidized beds for

---

[*] Corresponding author.
E-mail address: peter.loutzenhiser@me.gatech.edu (P.G. Loutzenhiser).

http://dx.doi.org/10.1016/j.fuel.2017.09.059
Received 20 July 2017; Received in revised form 5 September 2017; Accepted 13 September 2017

Nomenclature

D	distance traveled by ray
$\hat{e}$	unit vector
h	height
i	surface indices
n	moles
$\hat{n}$	unit normal vector
P	P-value
Q	heat
$\bar{r}$	energy bundle vector
$\bar{r}_0$	starting point vector
$\bar{r}_s$	surface vector
R	cold gas ratio
Re	Reynolds number
$\hat{s}$	unit vector along the path of the energy bundle
t	time
T	temperature
u	velocity
V	volume
x	distance (Cartesian)
X	carbon conversion
y	distance (Cartesian)
z	distance (Cartesian)
Greek	
ε	emissivity, void fraction
η	efficiency
λ	wavelength
ρ	density
υ	surface parameter

solar gasification of coal, cokes, and cellulose have been explored in literature [12,21–28]. One drawback of fluidized-bed designs compared to packed beds is that small, relatively uniform feedstock particles are required, translating to costlier feedstock preparation. The continuous nature of fluidized beds where inputs can be adjusted in response to disturbances (*e.g.*, solar irradiance) makes the design applicable for a hybrid solar/autothermal system. Experimental investigations of indirectly-irradiated fluidized beds are lacking in literature [31], with only one study that used steel for the emitter tube material [12].

In the present study, a novel 1.5 kW_{th} hybrid solar/autothermal gasifier was designed, fabricated, and tested in a 6 kW_{th} high-flux solar simulator (HFSS) [32]. The HFSS provides an external source of intense thermal radiation, mostly in the visible and IR spectra, closely approximating the heat transfer characteristics of high solar concentrating facilities. Monte Carlo (MC) ray-tracing analysis was performed to optimize the geometry of the gasifier for maximum absorption of concentrated irradiation. During testing, factors were varied at two levels: (1) H_2O:C ratio (1.1–2.32), feedstock type (activated charcoal and lignite coal), and O_2:C ratio (0–0.33). Time-averaged responses were evaluated in terms of average bed temperature, carbon conversion, cold gas (upgrade) ratio, solar-to-fuel efficiency, H_2:CO ratio, and CO_2 production. Statistical analyses were performed using analysis of variance (ANOVA) to identify significant effects and interactions on response variables.

2. Experimental setup

Experimentation was performed in a novel hybrid solar/autothermal gasifier designed to run continuously in both solar and combined solar/autothermal gasification modes. A fluidized-bed design was implemented, as it allowed for both modulation of feedstock inputs and increased residence times for high conversions of feedstock to syngas. An indirectly-irradiated gasifier was used to avoid the use of a window, eliminating the possibility of failure or fouling during operation in combined solar/autothermal gasification.

A schematic of the gasifier is given in Fig. 1a. The gasifier consisted of a cavity that was constructed from Buster M-35 (Zircar Zirconia) blocks, composed of Al_2O_3-SiO_2 insulation with low thermal conductivity, high operating temperature, and high reflectivity [33]. The cavity was used to capture multiple reflections and emissions while minimizing re-radiation losses to the environment and was held together with a stainless steel casing with dimensions of $210 \times 215 \times 275\ mm^3$. The front block contained a 40-mm diameter conical aperture with an acceptance angle of 45°. An absorber tube made of pressureless sintered SiC (Saint-Gobain Ceramics, Hexoloy SA) was positioned inside the cavity and had inner and outer diameters of 42 mm and 52 mm, respectively, and length of 300 mm. SiC was used due to durability at high temperatures, low coefficient of thermal expansion, and high thermal conductivity. Its high strength and chemical inertness

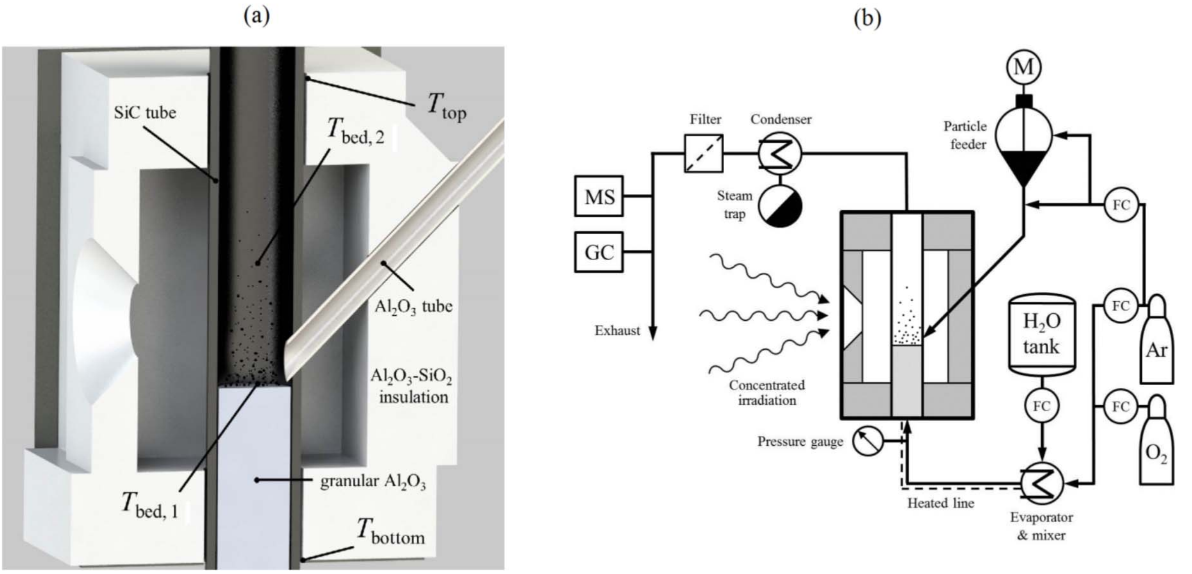

Fig. 1. Hybrid solar/autothermal gasifier (a) schematic and (b) process flow diagram.

make the material ideal for concentrated solar applications. The particular SiC used was a single phase composition with no free Si; the formation of a protective SiO_2 coating on the surface allowed it to remain stable at high temperatures [34]. The SiC tube was fabricated with a 45° 16.7-mm diameter angled hole in the back to allow for a feedstock delivery from a gravity-driven particle feeder (LAMBDA Instruments, DOSER) through an Al_2O_3 tube. The emitter tube contained a bed of Al_2O_3 granules (Micron Metals, 99.9% purity, 30–50 mesh) supported by a 72-mesh stainless steel screen.

Sheathed K-type thermocouple probes (OMEGA) were placed at two locations in the bed: (1) ~30 mm below the focal point at the tube center line (at the surface of the inert bed) and (2) ~30 mm above the focal point at the tube center line (in the region where particles would be fluidized). Two more K-type thermocouples were positioned on the outside of the emitter tube on the top and bottom. Continuous water cooling using coiled copper tubing was employed to prevent overheating at the top and bottom of the emitter tube due to the high thermal conductivity of SiC.

A process flow diagram of the gasifier setup is shown in Fig. 1b. Ar and O_2 flow rates were controlled using mass flow controllers (Bronkhorst, EL-FLOW), and a pressurized tank and liquid flow controller (Bronkhorst, Mini CORI-FLOW) was used to deliver $H_2O(l)$ to an evaporator (Bronkhorst, CEM), where it was mixed with the reacting gas flow. The particle feeder was purged with Ar in the feedstock vessel and just below the feeder at a constant rate of 2 L_N/min to prevent backflow of reacting gases. The feeder was calibrated with the purge Ar to a feeding rate of ~60 g/h. Based on the series of 15-min calibration tests, the feeding rates with 95% confidence intervals were 57.5 ± 2.7 and 62.3 ± 8.81 g/h for activated charcoal and lignite coal, respectively. Lignite was more difficult to flow consistently due to a smaller average particle size and greater cohesion between particles. A pressure gauge below the bed was used to monitor the temporal pressure inside of the gasifier. The gas stream leaving the gasifier passed through dry ice to condense out the water vapor from the flow, and a particle filter was installed to remove particles > 40 µm. Product gases were temporally monitored with a combination of mass spectrometry (MS, OmniStar ThermoStar GSD320 Gas Analysis System) and gas chromatography (GC, Agilent 490 Micro GC equipped with Molsieve and PoraPLOT Q columns). The GC was calibrated for H_2, CO, CO_2, CH_4, and O_2.

The feedstocks examined were granular activated charcoal derived from peat (Sigma-Aldrich, untreated powder, 20–60 mesh) and North Dakota lignite coal (40–60 mesh). Proximate and ultimate analyses given in Table 1 indicated that feedstocks can be described by simplified chemical formulas of $CH_{0.128}O_{0.054}$ and $CH_{0.754}O_{0.370}$ for activated charcoal and lignite coal, respectively. The pretreatment process for activated charcoal left a carbon-rich material with low volatile and moisture contents. Lignite coal had a much lower fixed carbon content and much higher volatile matter with some ash present in both samples. The LHV was calculated for both feedstocks based on correlations found in literature [35,36]. In an industrial-scale application, the feedstock would likely not be pre-pyrolyzed due to energy costs. For this reason, the lignite coal was more representative of what would be used in a scaled-up process.

Fused Al_2O_3 granules were used in the fluidized bed for support of any unreacted particles and partially fluidized in the bed. The low thermal conductivity of the Al_2O_3 granules also allowed the reacting gases to be preheated before reaching the bed surface without transferring significant heat from the reaction zone to the supportive stainless steel mesh.

3. Modeling

3.1. Radiation modeling

MC ray-tracing analysis was used to model the radiative exchange within the gasifier and optimize the geometry of the cavity. The medium inside of the gasifier cavity, air, was considered to be non-participating. The surfaces of the gasifier and cavity were considered to be opaque with spectral properties that were independent of temperature.

Concentrated irradiation was partitioned into 64 million energy packets (rays) with positional and directional vectors determined from an in-house MC ray-tracing analysis of the HFSS to model all seven xenon arc lamps mounted in truncated ellipsoidal reflectors [32]. The path of the energy bundle was determined in vector form, given as:

$$\bar{r} = \bar{r}_0 + D\hat{s} \tag{1}$$

where $\bar{r}_0$ represents the starting point of the energy bundle; D represents the distance traveled by an energy bundle; and $\hat{s}$ is the unit vector along the path of the energy bundle. Rigorous calorimetry coupled to modeling was used to determine total incoming radiative flow of 6.132 kW_{th} entering through the 40 mm diameter aperture [32]. The spectral distribution of the radiation was determined according to Planck's spectral distribution of blackbody emissive power, assuming a refractive index of unity. All of the surface within the gasifier exposed to the concentrated irradiation, including the inner cavity and outer SiC tube, were generically defined in vector form pointing from (0,0,0) on a global coordinate system [37], given as:

$$\begin{gathered}\bar{r}_0 = \sum_{i=1}^{3} x_i(\upsilon_1,\upsilon_2)\hat{e}_i,\\ \upsilon_{1,\min} \leqslant \upsilon_1 \leqslant \upsilon_{1,\max}, \upsilon_{2,\min}(\upsilon_1) \leqslant \upsilon_2 \leqslant \upsilon_{2,\max}(\upsilon_1)\end{gathered} \tag{2}$$

where υ_1 and υ_2 are two geometry-dependent parameters; x_i are the (x, y, z) coordinates of the surface point; and $\hat{e}_i$ are the unit vectors ($\hat{\imath}$, $\hat{\jmath}$, $\hat{k}$) in the x, y, z directions, respectively. $\bar{r}_s$ was chosen based on surface orientation. $\bar{r}_s$ was defined for the outer surface of the SiC tube as:

$$\begin{gathered}\bar{r}_s = [r_{cyl}\cos\upsilon_1 + x_{cyl}]\hat{i} + [r_{cyl}\sin\upsilon_1 + y_{cyl}]\hat{j} + [\upsilon_2 + z_{cyl}]\hat{k},\\ 0 \leqslant \upsilon_1 \leqslant 2\pi \text{ and } 0 \leqslant \upsilon_2 \leqslant h_{cyl}\end{gathered} \tag{3}$$

where r_{cyl} and h_{cyl} are the radius and height of the cylinder, respectively. Coordinates (x_{cyl}, y_{cyl}, z_{cyl}) define a point at the bottom, center of the cylinder in the world coordinates. $\bar{r}_s$'s were defined for the remaining surfaces in the cavity, and all surfaces were divided up into a number of subsurfaces. Intersections were determined for each incoming energy bundle to the nearest surface, and optical properties were introduced to determine whether the energy bundle was reflected or absorbed by the surface. For reflected energy bundles, a relative orthogonal coordinate system was created at the intersection, and the direction of the exiting energy bundle was determined assuming diffuse surfaces along with the relative orthogonal coordinate system. The choice of material had a significant effect on the captured radiation due to spectrally-dependent surface properties. The material selected for the gasifier cavity was M-35. The spectral properties of M-35 were assumed to be the same as Al_2O_3 due to the high Al_2O_3 content in M-35. The

Table 1
Proximate and ultimate analyses of feedstocks (values in weight% unless otherwise noted).

	Activated Charcoal	Lignite Coal
Carbon	84.01	55.60
Hydrogen	0.90	3.52
Nitrogen	0.37	0.75
Oxygen (BD)	6.09	27.37
Sulfur	0.25	1.54
Ash	8.38	11.22
Moisture	3.74	9.65
Volatile matter	4.94	37.88
Fixed carbon	82.94	41.25
H/C [mol/mol]	0.128	0.754
O/C [mol/mol]	0.054	0.370
LHV [MJ/kg]	29.3	19.4

spectral hemispherical emissivity of Al_2O_3 as a function of wavelength was obtained from experimentally-measured values [38]. A gray-band approximation was used for the MC ray-tracing, with wavelength bands of 0–5, 5–12 and 12-∞ μm. The lower emissivity at shorter wavelengths ($\lambda < 5$ μm) allowed the walls to reflect a significant amount of the incoming radiation, as > 98% of energy emitted by the sun falls in this wavelength range. At longer wavelengths, Al_2O_3 exhibits an emissivity close to unity. Experimental measurements for optical properties at high temperatures (> 1000 K) showed that the spectral hemispherical emissivity of SiC was almost constant over the wavelengths of interest and generally varied between $\varepsilon_\lambda = 0.90$ and 0.96 [39]. For this reason, the MC model used a total, hemispherical emissivity of $\varepsilon = 0.93$. A diffuse-gray approximation for SiC emissivity was applied to MC ray-tracing in a previous study [9]. The Al_2O_3 walls were rough and porous, which led to highly-diffuse reflections, and the SiC tube also had a relatively rough, dull surface, causing diffuse reflections. For this reason, reflection mode was set to diffuse for all surfaces in the gasifier. A series of parametric studies were run to examine the effect of prototype geometry and lamp configuration on heat flux distribution.

To determine the optimal lamp usage, three different configurations of lamps were tested with the tube placed at the center of the cavity. Symmetrical irradiation was desirable for enhanced heat transfer, so use of one side lamp necessitated the use of the opposing side lamp (*e.g.*, bottom-left and bottom-right lamps). Investigations focused on the use of the center and bottom lamps. The three cases simulated were two lamps (bottom and center), three lamps (bottom-left, bottom-right, and center), and four lamps (bottom-left, bottom-right, bottom, and center). The number of lamps had a clear effect on heat flux, creating absorbed powers and heat fluxes that were almost twice as high for four lamps compared to two. It was determined that using more than two lamps would likely cause excessive temperatures and problematic thermal stresses at the focus, so further simulations were run using only two lamps. Furthermore, use of two lamps on the same vertical axis was conducive to efficiently heating a vertical-tube configuration while minimizing losses to the cavity walls.

Three different positions of the emitter tube, measured from the center of the tube to the aperture: 35, 55, and 75 mm, were tested to examine the effect of distance. The model predicted the incident radiative flux and did not account for re-radiation losses (*i.e.*, surface emissions from the inside of the cavity), which would be significant at high temperatures. The absorbed irradiation by the tube did not vary significantly between the three cases, and slightly increased for the distance furthest from the front of the cavity. This is potentially a result of the reflected rays staying within the cavity due to the smaller view factor between the tube and the aperture. The farthest tube distance had significantly more diffuse irradiation and the largest heated area. As the tube was moved closer to the aperture, the heat flux became more circular and concentrated at the center of the tube. As with using more lamps, positioning the tube closer to the aperture created highly localized heat fluxes that could have caused steep temperature gradients and thermal stresses. Therefore, a position halfway between the center and far distances, 65 mm, was selected for the gasifier.

The final conditions used the center and top lamps, which shifted the heated portion of the tube downward. Because the inside of the tube contained gases flowing upward and a bed of inert and reacting particles at the bottom, heating a lower portion of the tube was favorable for endothermic gasification reactions. Fig. 2 shows the calculated heat flux distribution on the front of the tube using the center and top lamp. The total radiative heat flow absorbed by the tube was 408 W. The peak and average heat fluxes across a 40 × 40 mm^2 area at the center of the tube were 468 kW/m^2 and 139 kW/m^2 in this configuration, respectively.

3.2. Fluidized bed modeling

The fluidization properties for both the inert bed material and feedstock were modeled using various assumptions and correlations. A number of different fluidization regimes were considered, including bubbling, turbulent, and fast regimes [40]. An analysis was performed in order to put bounds on the conditions that would lead to particle fluidization and entrainment. The Ergun correlation [41] was used to calculate minimum fluidization velocity, u_{mf}.

Solid and bulk densities were measured and calculated using water displacement or provided by the manufacturer. Particle sphericity was estimated to be 0.70 for all materials based on values reported in literature for similar materials [42,43]. Fluid viscosity was estimated to be 62.81×10^{-6} Pa s based on Ar at 1200 K and atmospheric pressure, provided in literature [44]. The gases were assumed to behave ideally at 1200 K and 1 bar, and plug flow was assumed for the fluid phase. Void fraction at minimum fluidization, ε_{mf}, was calculated using the correlation from Broadhurst and Becker [45]. Terminal velocity, u_t, was calculated using correlations from Kunii and Levenspiel [46]. From u_t and u_{mf}, corresponding volumetric flow rates for the tube geometry were calculated.

The results from the fluidization calculations are shown in Table 2 for different ranges based on the minimum and maximum particle diameter. Relatively low volumetric gas flows were necessary to begin to fluidize the charcoal particles in the tube (< 5 L/min), while only very high velocities would enable entrainment of the inert bed material, 20.72 L/min of Ar flow would entrain the smallest activated charcoal particles out of the tube. The particle losses were mitigated by both the larger diameter and lower temperatures downstream of the emitter tube. However, particle feedstocks begin to shrink during the reaction and were more likely to be entrained out of the tube. Therefore, the experiments were designed to keep the total gas flow towards the lower end of the volumetric flow rate ranges shown in Table 2.

4. Results

A HFSS was used to provide radiative heat fluxes similar to what can be achieved in a heliostat field solar power tower configuration. A Lambertian target along with a CCD camera were used to measure pixel intensities that were correlated with spatial radiative heat fluxes [32]. Fig. 3 shows the measured radiative flux distribution at the aperture during the last stage of HFSS operation, with heat fluxes given in kW/m^2. Total power entering the aperture was found to be 1371.2 ± 6.4 W. Average heat flux across the same area was 1091 kW/m^2. Peak fluxes of ~1400 kW/m^2 were observed at the center of the aperture area, with fluxes decreasing to between 600 and 1000 kW/m^2 at the edges of the aperture area. Higher flux

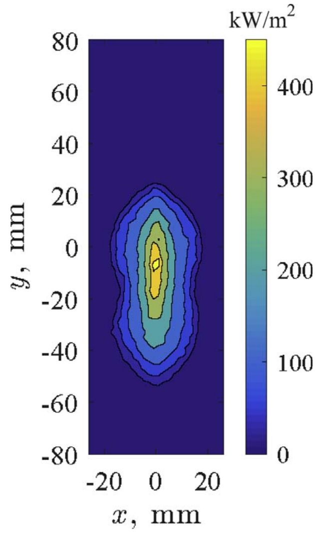

Fig. 2. Calculated radiative heat flux distribution in kW/m^2 on the front of the emitter tube for a distance of 65 mm from the aperture and using the top and center lamps.

Table 2
Results and related properties for the fluidization calculations for the particulate used in the fluidized bed during experimentation in the hybrid solar/autothermal gasifier.

	Granular Al_2O_3	Activated charcoal	Lignite coal
Particle diameter (mm)	0.297–0.595	0.250–0.841	0.250–0.425
ρ_{bulk} (g/ml)	1.87	0.27	0.86
$\rho_{particle}$ (g/ml)	3.97	0.46	0.95
ε_{mf} (−)	0.51–0.55	0.56–0.62	0.57–0.60
u_{mf} (m/s)	0.064–0.200	0.009–0.064	0.016–0.037
Re_{mf} (-)	0.123–0.769	0.015–0.347	0.026–0.102
u_t (m/s)	3.034–6.058	0.249–2.820	0.516–1.490
$\dot{V}_{mf}$ (L/min)	5.31–16.61	0.75–5.31	1.31–3.09
$\dot{V}_t$ (L/min)	252.2–503.5	20.72–234.4	42.85–123.8

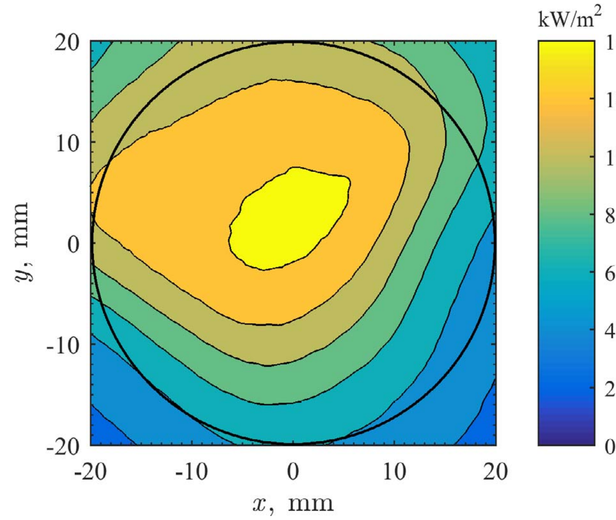

Fig. 3. Measured radiative heat flux map in kW/m^2 for the aperture during the last stage of high-flux solar simulator operation, with the aperture shape indicated by the black circle.

concentrations were observed at the top of the aperture area, likely due to the use of the top lamp. The radiation entering the aperture would be more diffuse upon reaching the emitter tube.

Experimental conditions are provided in Table 3 for both activated charcoal and lignite coal where the experimental design allowed for two 2^2 statistical analyses. The first two-way ANOVA compared the effects of H_2O:C and O_2:C (both for activated charcoal), and the second two-way ANOVA compared the effects of H_2O:C and feedstock (both at the zero O_2 condition). Two replicates of each experiment were run, resulting in 12 total experiments. Feeder vessel purge Ar flow for each experiment was 2 L_N/min, but gasifier inlet flows of Ar were adjusted to maintain a constant total volumetric flow rate consistent for given feedstocks. The total Ar concentration was maintained at ≥50% to keep product gases relatively dilute. The total gas flow was 7.5 L_N/min for the activated charcoal experiments but was lowered to ~5 L_N/min for the lignite coal experiments to adjust for smaller particles and associated entrainment. A thermocouple was placed at the tube outlet centerline measured an approximate steady-state temperature of ~900 K prior to particle feeding. This led to entrainment of some of the smaller charcoal particles, observed in the outlet flange after each experiment in amounts of a few grams or less.

The H_2O levels were chosen such that the average H_2O:C ratio would be greater than stoichiometrically required according to feedstock C content from the proximate and ultimate analyses. For the low H_2O experiments, the average H_2O:C ratios were between 1.10 and 1.16, and for the high H_2O experiments, the average H_2O:C ratio were between 2.20 and 2.32. The O_2 levels were chosen to ensure only a small portion of the feedstock was combusted; only 0.5 L_N/min O_2 was introduced for the experiments with O_2 (combined solar/autothermal). This corresponded to an average O_2:C ratio of 0.33, meaning that approximately one-third of the feedstock would be combusted. H_2O condensed out of the product gas stream ranged between ~10 and 30 ml depending on experimental conditions.

Representative runs are shown in Figs. 4 and 5 for experiments without and with O_2 for activated charcoal, respectively. Fig. 4a shows temporal temperatures, concentrated solar irradiation entering the aperture, and Fig. 4b shows product gas molar flows for a high H_2O run without O_2. Prior to lamp firing, Ar flow was initiated per the experimental conditions. The evaporator was heated to 473 K, and the heat tape around the gas line to the gasifier was turned on. Cooling water flow was introduced to the top and bottom of the emitter tube. The center lamp was turned on at $t = 0$, followed by the top lamp at $t = 10$ min. At $t \sim 20$ min, the center lamp was increased to close to full power. After the temperatures reached an approximate steady state at $t \approx 30$ min, $H_2O(v)$ was introduced to the system at the desired level depending on the experiment. The surface of the inert bed reached ~1230 K prior to charcoal feeding. At $t = 35$ min, charcoal feeding began at ~57.5 g/h. Charcoal feeding proceeded for 15 min. After the charcoal feeding commenced, the temperature at the surface of the bed ($T_{bed,1}$) dropped to ~1150 K, owing to the strongly-endothermic gasification reactions. The temperature ~60 mm above the surface of the bed ($T_{bed,2}$) stayed relatively constant at ~1170 K, indicative of particles settling on the surface of the bed that were undergoing conversion. After 15 min, $H_2O(v)$ and charcoal feeding were stopped and the lamps were turned off. For the lignite experiments, particle feeding proceeded for ~25 min to allow for a greater period of time-averaging due to less consistent flow. The gas temperature at the inlet of the gasifier was ~ 410 K during particle feeding. The pressure in the gasifier varied between 0 and 20 kPa depending on the stage of the experiment.

The associated product gas molar flows from GC showed a rapid rise in H_2, CO, and CO_2 after charcoal feeding began. Negligible CH_4 was observed, and no O_2 was detected during any of the runs. Small amounts of H_2 and CO were generated prior to charcoal feeding, likely due to residual charcoal particles in the bed. The gas composition began to level off ~7 min after charcoal feeding began. It was observed that while the relative amounts of H_2, CO, and CO_2 were similar to those predicted at chemical equilibrium, the relative amount of H_2 was less than what was predicted at chemical equilibrium. This observation points to a potential kinetic or mass transfer limitation.

The representative run with O_2 shown in Fig. 5 was performed at the low H_2O condition. Heat up showed conditions similar to those in Fig. 4a, including the initial temperature drop after the introduction of charcoal particles. For the experiments with O_2 flow, 0.5 L_N/min O_2 was added after $t = 2$ min of charcoal feeding, which again proceeded for 15 min. Once O_2 was introduced, there was a marked increase in $T_{bed,1}$ and $T_{bed,2}$. Prior to charcoal feeding, the $T_{bed,1}$ was at ~1240 K,

Table 3
Experimental conditions for testing in the high-flux solar simulator (concentrations of total gas flow including feeder purge are given in parentheses).

	Low H_2O	High H_2O
Without O_2 (act. char.)	84.3 g/h H_2O (23.3%) 0 L_N/min O_2 (0%) 3.75 + 2 L_N/min Ar (76.7%)	168.6 g/h H_2O (46.6%) 0 L_N/min O_2 (0%) 2 + 2 L_N/min Ar (53.4%)
With O_2 (act. char.)	84.3 g/h H_2O (23.3%) 0.5 L_N/min O_2 (6.7%) 3.25 + 2 L_N/min Ar (70.0%)	168.6 g/h H_2O (46.6%) 0.5 L_N/min O_2 (6.7%) 1.5 + 2 L_N/min Ar (46.7%)
Without O_2 (lignite)	58.0 g/h H_2O (24.5%) 0 L_N/min O_2 (0%) 1.7 + 2 L_N/min Ar (75.5%)	116.0 g/h H_2O (49.0%) 0 L_N/min O_2 (0%) 0.5 + 2 L_N/min Ar (51.0%)

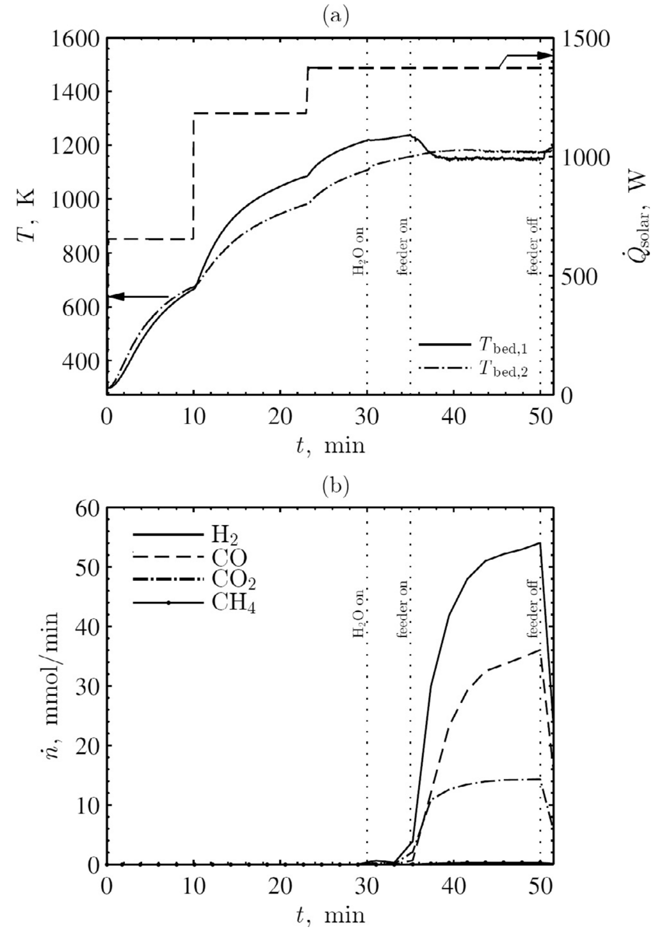

Fig. 4. Representative run for a condition without O_2 (solar-only) using activated charcoal. The run shown uses the high level of H_2O with (a) temporal bottom (dashed-dotted) and top (solid) bed temperatures and solar energy (dashed) entering aperture and (b) temporal product gas molar flows measured with gas chromatography for H_2 (solid), CO (dashed), CO_2 (dashed-dotted), and CH_4 (circle marker).

but it reached temperatures of ~1410 K after O_2 was introduced. $T_{bed,2}$ did not show as drastic of an increase, but a temperature rise of ~100 K was observed. As with the run without O_2, this indicates that most of the reactions were concentrated at the surface of the bed. Some ash melting was observed on the surface of the bed during gasifier cleaning in the runs with O_2,

The associated product gas molar flows again showed a rapid rise in H_2, CO, and CO_2 after charcoal feeding began. Negligible CH_4 was observed. After O_2 was introduced, H_2 and CO decreased, and then slowly began to rise again. As expected from equilibrium compositions, a larger amount of CO_2 was observed as compared to the runs without O_2 and H_2:CO ratio was less than unity. This could be a result of kinetically-rapid combustion reactions or the reverse water-gas shift reaction taking place downstream of the reaction zone prior to product gas sampling at lower temperatures.

An average bed temperature was calculated from $T_{bed,1}$ and $T_{bed,2}$. Average carbon conversion is represented as:

$$\bar{X} = \frac{\bar{\dot{n}}_{CO} + \bar{\dot{n}}_{CO_2} + \bar{\dot{n}}_{CH_4}}{\bar{\dot{n}}_C} \tag{4}$$

where $\bar{\dot{n}}_i$ represents the time-averaged molar flow of product *i*. $\bar{\dot{n}}_C$ was calculated based on the known feedstock composition and mass flow rate of the particle feeder. Average cold gas ratio, $\bar{R}$, is represented as:

$$\bar{R} = \frac{\bar{\dot{n}}_{products} LHV_{products}}{\bar{\dot{n}}_{feedstock} LHV_{feedstock}} \tag{5}$$

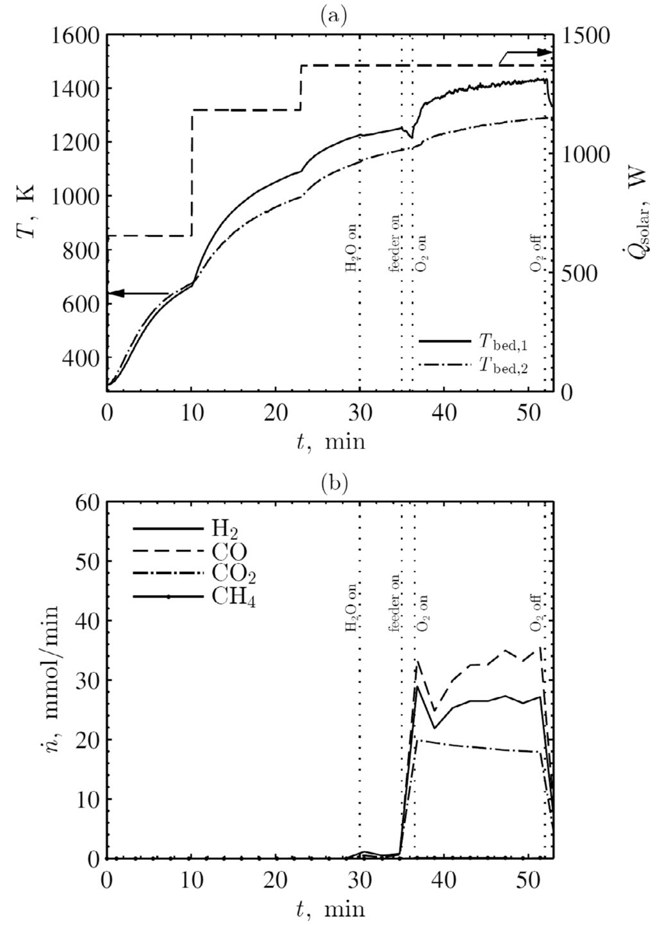

Fig. 5. Representative run for a condition with O_2 (combined solar/autothermal) using activated charcoal. The run shown used the low level of H_2O with (a) temporal bottom (dashed-dotted) and top (solid) bed temperatures and solar energy (dashed) entering aperture and (b) temporal product gas molar flows measured with gas chromatography for H_2 (solid), CO (dashed), CO_2 (dashed-dotted), and CH_4 (circle marker).

where the denominator represents energy content of the converted feedstock, and LHV is the lower heating value of each gaseous component on a molar basis. *LHV* of H_2, CO, and CH_4 are 120.0, 10.1, and 50.0 MJ/kg on a mass basis, respectively. Average solar-to-fuel efficiency, $\bar{\eta}_{\text{solar-to-fuel}}$, is similarly represented as:

$$\bar{\eta}_{solar-to-fuel} = \frac{\bar{\dot{n}}_{products} LHV_{products}}{\dot{Q}_{solar} + \bar{\dot{n}}_{feedstock} LHV_{feedstock}} \tag{6}$$

where $\dot{Q}_{solar}$ is the concentrated irradiation power into the aperture according to flux calibrations. The time averaged quantities are given in Table 4. A constant output of syngas was not possible for all cases, as steady conditions were not attained due to a buildup of the feedstock in the bed. For these cases, the $\bar{\eta}_{\text{solar-to-fuel}}$ was slightly lower than the $\eta_{\text{solar-to-fuel}}$ determined at the end of the run due to more syngas production.

Results showed good reproducibility between replicates and clear effects of reacting gas composition on product gas composition, temperature, conversion, cold gas ratio, and solar-to-fuel efficiency. Significant CH_4 was only observed in the experiments using lignite coal as the feedstock, possibly due to the higher volatile content and CH_4 being generated during pyrolysis. The highest $\bar{X} = 0.79$, were observed for the activated charcoal under the high H_2O:C conditions with O_2 where, presumably, full conversion did not occur due to entrainment of the smaller particles that did not fully react as observed after experimentation. The highest $\bar{R} = 1.16$ was observed for the lignite coal low H_2O:C condition, which corresponded to the lowest $\bar{X} = 0.55$. The

Table 4

A summary of results from experimentation in the hybrid solar/autothermal gasifier with feedstock of activated charcoal or lignite coal reacted with O_2 and/or mixtures of Ar and H_2O.

Feedstock	$\overline{H_2O:C}$ (−)	$\overline{O_2:C}$ (−)	$\bar{n}_{H_2}$ (mmol/min)	$\bar{n}_{CO}$ (mmol/min)	$\bar{n}_{CO_2}$ (mmol/min)	$\bar{n}_{CH_4}$ (mmol/min)	$\overline{H_2:CO}$ (−)	$\overline{T}_{bed,avg}$ (K)	$\overline{X}$ (−)	$\overline{R}$ (−)	$\bar{\eta}_{solar\text{-}to\text{-}fuel}$ (%)
Activated charcoal	1.16	0	42.8	35.4	8.0	0.2	1.21	1215	0.66	1.13	20.5
Activated charcoal	1.16	0	41.8	34.1	8.0	0.2	1.23	1183	0.64	1.13	19.9
Activated charcoal	1.16	0.33	26.9	33.6	18.9	0.1	0.80	1304	0.79	0.73	15.4
Activated charcoal	1.16	0.33	26.7	33.7	18.3	0.1	0.79	1343	0.79	0.74	15.4
Activated charcoal	2.32	0	51.9	30.9	15.1	0.3	1.68	1205	0.70	1.11	21.2
Activated charcoal	2.32	0	52.6	34.3	14.2	0.3	1.54	1163	0.74	1.11	22.1
Activated charcoal	2.32	0.33	28.5	23.7	22.8	0.1	1.20	1331	0.70	0.70	13.4
Activated charcoal	2.32	0.33	30.3	24.1	23.4	0.1	1.26	1326	0.72	0.72	13.9
Lignite coal	1.10	0	27.9	20	7.1	1.6	1.40	1264	0.60	1.14	14.5
Lignite coal	1.10	0	27.4	17.8	7.1	1.4	1.53	1299	0.55	1.16	13.7
Lignite coal	2.20	0	33.6	19.1	10.5	1.7	1.76	1274	0.65	1.13	15.6
Lignite coal	2.20	0	34.3	19.0	11.2	2.0	1.80	1252	0.67	1.13	16.0

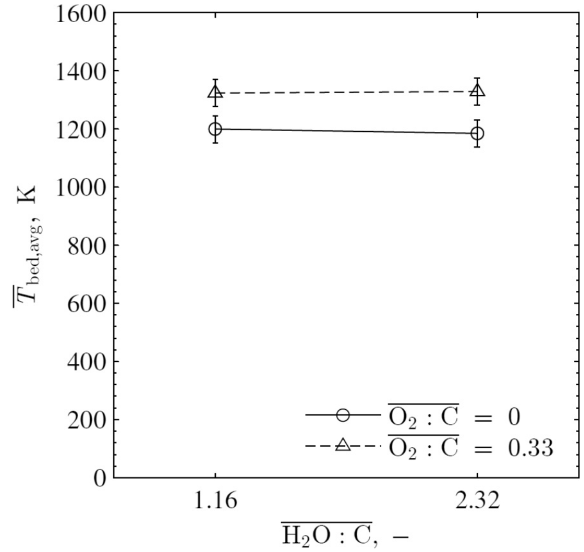

Fig. 6. Mean bed temperature versus mean H_2O to C ratio for mean O_2 to C ratios of 0 (circles) and 0.33 (triangles) using activated charcoal. The included error bars represent 95% confidence limits.

highest $\bar{\eta}_{solar-to-fuel} = 22.1\%$ was observed using the high H_2O:C condition with O_2 for activated charcoal. In order to more closely examine the main and interaction effects on each parameter, a series of ANOVA were performed using R statistical computing software [47] and interaction plots [48] were created for response variable means with error bars based on 95% confidence limits [49].

4.1. Two-way ANOVA for assessing effects of H_2O:C and O_2:C

The series of two-way ANOVA showed several significant effects and interactions for the activated charcoal. The response variables were $\overline{T}_{bed,avg}$, $\overline{X}$, $\overline{H_2:CO}$, $\bar{n}_{CO_2}$, $\overline{R}$, and $\bar{\eta}_{solar\text{-}to\text{-}fuel}$. Notably, $\overline{O_2:C}$ had a significant effect on all response variables. Increased O_2 was associated with increased $\overline{T}_{bed,avg}$ ($P < 0.01$), $\overline{X}$ ($P < 0.01$), and $\bar{n}_{CO_2}$ ($P < 0.0001$). Fig. 6 shows an interaction plot of $\overline{T}_{bed,avg}$ means, which illustrates that O_2 tends to raise bed temperatures due to strongly-exothermic combustion reactions. No interactions were observed for $\overline{T}_{bed,avg}$, and the parallel horizontal lines indicate that $\overline{H_2O:C}$ did not have a significant effect on$\overline{T}_{bed,avg}$. Variances in $T_{bed,avg}$ were possibly due to highly localized temperature fluctuations resulting from endothermic or exothermic reactions, as particles and reacting gases have constantly-changing distributions in a fluidized bed.

Increased O_2 was associated with decreased $\overline{H_2:CO}$ ($P < 0.001$), $\overline{R}$ ($P < 0.0001$), and $\bar{\eta}_{solar\text{-}to\text{-}fuel}$ ($P < 0.0001$). Introducing O_2 reduced energy content of the product gases and reduced utilization of solar energy. For F-T synthesis, the optimal H_2:CO ratio is 1.7–2.15 depending on the type of catalyst used [50], which indicates that the product gases would need to be water-gas shifted downstream in some cases based on experimental $\overline{H_2:CO}$.$\overline{H_2O:C}$ had significant effects on $\overline{R}$ ($P < 0.05$), $\overline{H_2:CO}$ ($P < 0.001$), $\bar{n}_{CO_2}$ ($P < 0.0001$). There was a slight decrease in $\overline{R}$ with increased H_2O. The increased $\overline{H_2:CO}$ and $\bar{n}_{CO_2}$ with higher levels of $\overline{H_2O:C}$ likely due to increased water-gas shift reactions. Significant interactions were observed between $\overline{O_2:C}$ and $\overline{H_2O:C}$ for $\overline{X}$ ($P < 0.01$), $\bar{n}_{CO_2}$ ($P < 0.05$), and $\bar{\eta}_{solar\text{-}to\text{-}fuel}$ ($P < 0.01$). Fig. 7 shows an interaction plot for $\overline{X}$ means. The plot shows the interaction between $\overline{O_2: C}$ and $\overline{H_2O:C}$, where introducing O_2 increased conversion for the low $\overline{H_2O:C}$ case, but not for the high $\overline{H_2O:C}$ case.

4.2. Two-way ANOVA for assessing effects of H_2O:C and feedstock

A series of two-way ANOVA were also used to determine significant effects and interactions for $\overline{H_2O:C}$ and feedstock, both at the low $\overline{O_2:C}$

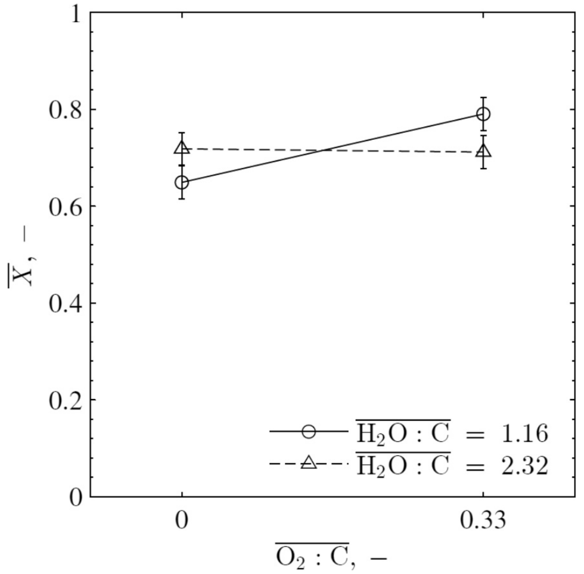

Fig. 7. Mean carbon conversion as a function of the mean O_2 to C ratio for the mean ratios of H_2O to C of 1.16 (circles) and 2.32 (triangles) with the error bars based on 95% confidence limits.

condition. Feedstock had a significant effect on all response variables: $\overline{T}_{bed,avg}$ ($P < 0.01$), $\overline{X}$ ($P < 0.05$), $\overline{H_2{:}CO}$ ($P < 0.01$), $\overline{\dot{n}}_{CO_2}$ ($P < 0.01$), $\overline{R}$ ($P < 0.05$), and $\overline{\eta}_{solar\text{-}to\text{-}fuel}$ ($P < 0.0001$). It is important to note that other changes were associated with the feedstock including particle size distribution and total gas flow rate. This changes sensible heat absorbed by the reacting gas as well as the likelihood of particle entrainment. Fig. 8 shows an interaction plot for $\overline{\eta}_{solar\text{-}to\text{-}fuel}$ means, which were notably higher for the activated charcoal experiments. There was a slight but statistically significant effect from $\overline{H_2O{:}C}$ ($P < 0.01$), with higher $\overline{H_2O{:}C}$ leading to greater $\overline{\eta}_{solar\text{-}to\text{-}fuel}$. There were also significant effects of $\overline{H_2O{:}C}$ on $\overline{X}$ ($P < 0.05$), $\overline{H_2{:}CO}$ ($P < 0.01$), $\overline{R}$ ($P < 0.05$), $\overline{\eta}_{solar\text{-}to\text{-}fuel}$ ($P < 0.0001$).

There was only one significant interaction of feedstock and $\overline{H_2O{:}C}$, which was for $\overline{\dot{n}}_{CO_2}$ ($P < 0.05$). Fig. 9 shows an interaction plot for $\overline{\dot{n}}_{CO_2}$ means. The higher $\overline{\dot{n}}_{CO_2}$ for the activated charcoal was expected, as more C was being fed into the gasifier. $\overline{\dot{n}}_{CO_2}$ did not increase as dramatically with $\overline{H_2O{:}C}$ for the lignite coal, as water gas shift reactions were less prominent with less available CO and H_2O. While reduced CO_2 generation is desirable in a gasification process, the lignite coal experiments also had reduced syngas production, negatively affecting process viability. These trade-offs would need to be weighed in an optimized, scaled-up solar process.

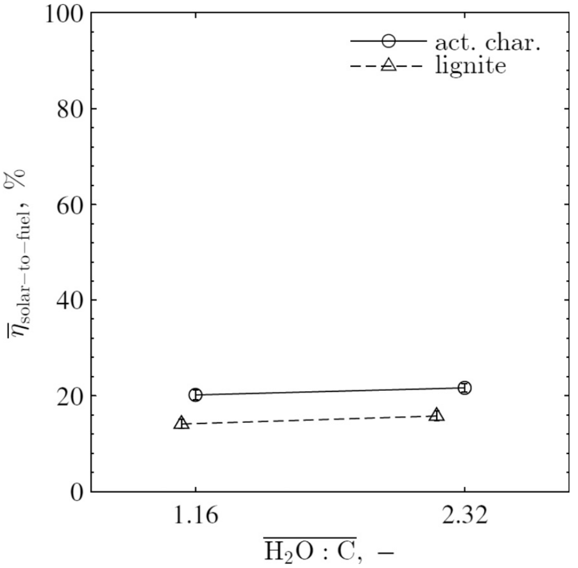

Fig. 8. Mean solar-to-fuel efficiency versus the mean ratio of H_2O to C for solar only operation with activated charcoal (circles) and lignite coal (triangles) and error bars based on 95% confidence limits.

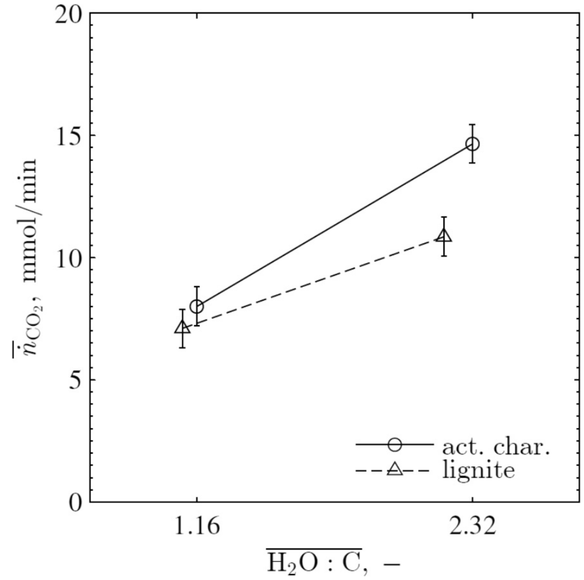

Fig. 9. Mean molar flow of CO_2 versus the mean ratio of H_2O to C for solar only operation with activated charcoal (circles) and lignite coal (triangles) and error bars based on 95% confidence limits.

5. Discussion

The results point to several notable effects from H_2O:C, O_2:C, and feedstock for a solar-driven gasification system. To the authors' knowledge, this is the first demonstration of a combined solar/autothermal gasification process, as well as the first indirectly-irradiated fluidized bed constructed out of SiC to be tested using concentrated irradiation. The system successfully created syngas and demonstrated temperature effects from the introduction of O_2, but has room for optimization to improve performance. Carbon conversions were slightly higher than those achieved by previous SiC drop-tube and entrained-flow experiments [8,10,11], and slightly lower than those achieved by a drop-tube fixed-bed gasifier [7]. Particle entrainment may have limited carbon conversions, even when using the lower flow rate for lignite coal experiments. Cold gas (upgrade) ratios and solar-to-fuel efficiencies were very similar to those achieved by the drop-tube fixed-bed gasifier [7]. These parameters could be improved by operating at higher temperatures, reducing the formation of CO_2, but that would come at the expense of increased re-radiation losses.

The observation that the bed temperature was significantly affected by O_2:C was expected, but it is noteworthy in its implications for a continuous hybrid solar/autothermal gasification process. The impact of O_2:C ratio on carbon conversion was also important, as it may allow for more rapid conversion and tuning of the feedstock amount within the gasifier due to fast combustion kinetics. The negative consequences of combustion were equally significant, with O_2:C reducing H_2:CO ratio, cold gas ratio, solar-to-fuel efficiency, and increasing CO_2 production. Therefore, O_2 use in a hybrid operation should be minimized and used only when required to maintain acceptable performance parameters.

Feedstock also significantly affected the response variables for solar-only operation, with the lower fixed-carbon feedstock generally having reduced performance. However, the cold gas ratio was slightly higher for lignite coal, possibly due to more CH_4 being generated with lower conversions that were compensated for by the reduced syngas output in the calculation. Nonetheless, the performance was acceptable using a more realistic feedstock, and the system could be improved to reduce particle entrainment. Ideally, a biomass feedstock would be used in a gasification process instead of a fossil fuel to reduce life-cycle CO_2 emissions, which would introduce additional challenges in terms of particle feeding and material processing.

The effects of changing H_2O level were less dramatic, but still important in the performance of a hybrid gasification process. The most significant effect was tied to the water-gas shift reaction, affecting both H_2:CO and CO_2 production. These effects were antagonistic: improved H_2:CO ratios for F-T synthesis comes at the expense of increased CO_2 production. A far less notable impact was seen on cold gas ratio, with slight decreases as H_2O:C increased. The significant interactions for carbon conversion, CO_2 production, cold gas ratio, and solar-to-fuel efficiency point to a complex interplay between reacting gases that requires further analysis. For the purposes of process control, H_2O represents a tunable parameter in addition to O_2 that can be adjusted per solar resource availability or desired H_2:CO ratio.

6. Conclusions

A novel 1.5 kW_{th} scale hybrid solar/autothermal gasifier was designed and tested in a high-flux solar simulator in solar and combined solar/autothermal modes. Monte Carlo ray-tracing was performed to evaluate resulting heat fluxes for various tube positions and lamp configurations. A bench-scale indirectly-irradiated fluidized-bed gasifier was designed and fabricated using materials suitable for solar thermochemical applications. The design of the gasifier allowed for long residence times, high gas-solid contact, continuous operation, and adjustment of feedstock flow rate. Carbon conversions of up to 0.79 were observed, and maximum cold gas ratios and solar-to-fuel efficiencies were 1.16 and 22.1%, respectively.

The experimental campaign demonstrated the ability to feed small streams of pure O_2 into a solar gasifier to increase temperatures. In this way, transient deficits in solar energy that are inherent in solar gasification may be overcome. Future work may focus on dynamically-controlling inlet flows based on solar input to maintain high temperatures, showing the possibility of continuous operation while still obtaining the benefits of a solar-driven process.

Acknowledgements

This material is based on work supported by the National Science Foundation – United States Graduate Research Fellowship under Grant DGE-1148903.

References

[1] Muroyama A, Shinn T, Fales R, Loutzenhiser PG. Modeling of a dynamically-controlled hybrid solar/autothermal steam gasification reactor. Energy Fuels 2014;28(10):6520–30.
[2] Muroyama AP, Loutzenhiser PG. Kinetic analyses of gasification and combustion reactions of carbonaceous feedstocks for a hybrid solar/autothermal gasification process to continuously produce synthesis gas. Energy Fuels 2016;30(5):4292–9.
[3] Kaniyal AA, van Eyk PJ, Nathan GJ. Dynamic modeling of the coproduction of liquid fuels and electricity from a hybrid solar gasifier with various fuel blends. Energy Fuels 2013;27(6):3556–69.
[4] Kaniyal AA, van Eyk PJ, Nathan GJ, Ashman PJ, Pincus JJ. Polygeneration of liquid fuels and electricity by the atmospheric pressure hybrid solar gasification of coal. Energy Fuels 2013;27(6):3538–55.
[5] Loutzenhiser PG, Muroyama AP. A review of the state-of-the-art in solar-driven gasification processes with carbonaceous materials. Sol Energy 2017.
[6] Z'Graggen A, Steinfeld A. Radiative exchange within a two-cavity configuration with a spectrally selective window. J Sol Energy Eng Trans-ASME 2004;126:819–22.
[7] Kruesi M, Jovanovic ZR, Steinfeld A. A two-zone solar-driven gasifier concept: Reactor design and experimental evaluation with bagasse particles. Fuel 2014;117(Part A):680–7.
[8] Martinek J, Bingham C, Weimer AW. Computational modeling of a multiple tube solar reactor with specularly reflective cavity walls. Part 2: steam gasification of carbon. Chem Eng Sci 2012;81:285–97.
[9] Martinek J, Bingham C, Weimer AW. Computational modeling and on-sun model validation for a multiple tube solar reactor with specularly reflective cavity walls. Part 1: heat transfer model. Chem Eng Sci 2012;81:298–310.
[10] Lichty P, Perkins C, Woodruff B, Bingham C, Weimer A. Rapid high temperature solar thermal biomass gasification in a prototype cavity reactor. J Sol Energy Eng Trans-ASME 2010;132(1).
[11] Melchior T, Perkins C, Lichty P, Weimer AW, Steinfeld A. Solar-driven biochar gasification in a particle-flow reactor. Chem Eng Process 2009;48(8):1279–87.
[12] Murray JP, Fletcher EA. Reaction of steam with cellulose in a fluidized bed using concentrated sunlight. Energy 1994;19(10):1083–98.
[13] Piatkowski N, Steinfeld A. Solar-driven coal gasification in a thermally irradiated packed-bed reactor. Energy Fuels 2008;22:2043–52.
[14] Piatkowski N, Steinfeld A. Solar gasification of carbonaceous waste feedstocks in a packed-bed reactor—dynamic modeling and experimental validation. Aiche J 2011;57(12):3522–33.
[15] Piatkowski N, Weickert C, Steinfeld A. Experimental investigation of a packed-bed solar reactor for the steam-gasification of carbonaceous feedstocks. Fuel Process Technol 2009;90:360–6.
[16] Müller F, Poživil P, van Eyk PJ, Villarrazo A, Haueter P, Wieckert C, et al. A pressurized high-flux solar reactor for the efficient thermochemical gasification of carbonaceous feedstock. Fuel 2017;193:432–43.
[17] Hathaway BJ, Davidson JH. Demonstration of a prototype molten salt solar gasification reactor. Sol Energy 2017;142:224–30.
[18] Z'Graggen A, Haueter P, Trommer D, Romero M, de Jesus JC, Steinfeld A. Hydrogen Production by Steam-Gasification of Petroleum Coke Using Concentrated Solar Power—II Reactor Design, Testing, and Modeling. Int J Hydrogen Energy 2006;31(6):797–811.
[19] Gregg DW, Taylor RW, Campbell JH, Taylor JR, Cotton A. Solar gasification of coal, activated carbon, coke and coal and biomass mixtures. Sol Energy 1980;25(4):353–64.
[20] Wieckert C, Obrist A, Zedtwitz PV, Maag G, Steinfeld A. Syngas Production by Thermochemical Gasification of Carbonaceous Waste Materials in a 150 kW_{th} Packed-Bed Solar Reactor. Energy Fuels 2013;27(8):4770–6.
[21] Abe T, Gokon N, Izawa T, Kodama T. Internally-circulating fluidized bed reactor using thermal storage material for solar coal coke gasification. Energy Procedia 2015;69:1722–30.
[22] Gokon N, Izawa T, Abe T, Kodama T. Steam gasification of coal cokes in an internally circulating fluidized bed of thermal storage material for solar thermochemical processes. Int J Hydrogen Energy 2014;39(21):11082–93.
[23] Gokon N, Izawa T, Kodama T. Steam gasification of coal cokes by internally circulating fluidized-bed reactor by concentrated Xe-light radiation for solar syngas production. Energy 2015;79:264–72.
[24] Gokon N, Ono R, Hatamachi T, Liuyun L, Kim H-J, Kodama T. CO2 gasification of coal cokes using internally circulating fluidized bed reactor by concentrated Xe-light irradiation for solar gasification. Int J Hydrogen Energy 2012;37(17):12128–37.
[25] von Zedtwitz P, Lipinski W, Steinfeld A. Numerical and experimental study of gas-particle radiative heat exchange in a fluidized-bed reactor for steam-gasification of coal. Chem Eng Sci 2007;62:599–607.
[26] von Zedtwitz P, Steinfeld A. Steam-gasification of coal in a fluidized-bed/packed-bed reactor exposed to concentrated thermal radiation modeling and experimental validation. Ind Eng Chem Res 2005;44(11):3852–61.
[27] Müller R, von Zedtwitz P, Wokaun A, Steinfeld A. Kinetic investigation on steam gasification of charcoal under direct high-flux irradiation. Chem Eng Sci 2003;58(22):5111–9.
[28] Taylor RW, Berjoan R, Coutures JP. Solar gasification of carbonaceous materials. Sol Energy 1983;30(6):513–25.
[29] Hathaway BJ, Davidson JH, Kittelson DB. Solar gasification of biomass: kinetics of pyrolysis and steam gasification in molten salt. J Sol Energy Eng Trans-ASME 2011;133:9.
[30] Hathaway BJ, Honda M, Kittelson DB, Davidson JH. Steam gasification of plant biomass using molten carbonate salts. Energy 2013;49:211–7.
[31] Puig-Arnavat M, Tora EA, Bruno JC, Coronas A. State of the art on reactor designs for solar gasification of carbonaceous feedstock. Sol Energy 2013;97:67–84.
[32] Gill R, Bush E, Haueter P, Loutzenhiser P. Characterization of a 6 kW high-flux solar simulator with an array of xenon arc lamps capable of concentrations of nearly 5000 suns. Rev Sci Instrum 2015;86(12):125107.
[33] Zircar Zirconia Inc. Buster - High Temperature Alumina Insulation; 2017. Available from: https://zircarzirconia.com/wp-content/uploads/2017/05/ZZ-5200-Rev01-Buster.pdf.
[34] Saint-Gobain Ceramics. Hexoloy SA Silicon Carbide - Technical Data; 2012. Available from: http://www.refractories.saint-gobain.com/sites/imdf.hpr.com/files/hexoloy-sa-sic-tds_0.pdf.
[35] Channiwala SA, Parikh PP. A unified correlation for estimating HHV of solid, liquid and gaseous fuels. Fuel 2002;81(8):1051–563.
[36] Eggleston HS, Buendia L, Miwa K, Ngara T, Tanabe K. Guidelines for National Greenhouse Gas Inventories. 2. Japan: IPCC; 2006.
[37] Modest MF. Radiative heat transfer. United States of America: Academic Press; 2003.
[38] Touloukian YS, DeWitt DP. Thermal radiative properties: nonmetallic solids. New York: IFI/Plenum; 1972.
[39] Neuer G. Spectral and total emissivity measurements of highly emitting materials. Int J Thermophys 1995;16(1):257–65.
[40] Levenspiel O. Chemical reaction engineering. 3rd ed. Wiley; 1999.
[41] Ergun S. Fluid flow through packed columns. Chem Eng Prog 1952;48:89–94.
[42] Clements M, Haarhoff J. Practical experiences with granular activated carbon

(GAC) at the Rietvlei Water Treatment Plant. Water SA 2004;30(1):89–96.
[43] Yang WC. Handbook of Fluidization and Fluid-Particle Systems. Taylor & Francis; 2003.
[44] Bich E, Millat J, Vogel E. The viscosity and thermal conductivity of pure monatomic gases from their normal boiling point up to 5000 K in the limit of zero density and at 0.101325 MPa. J Phys Chem Ref Data 1990;19(6):1289–305.
[45] Broadhurst TE, Becker HA. Onset of fluidization and slugging in beds of uniform particles. Aiche J 1975;21(2):238–47.
[46] Kunii D, Levenspiel O. Fluidization Engineering. Butterworth-Heinemann; 1991.
[47] McFarland JA, Greenough JA, Ranjan D. Simulations and analysis of the reshocked inclined Interface Richtmyer-Meshkov instability for linear and nonlinear interface perturbations. J Fluids Eng 2014;136(7):071203.
[48] Wu CFJ, Hamada MS. Experiments: planning, analysis, and optimization. Wiley; 2011.
[49] Vardeman SB, Jobe JM. Basic Engineering Data Collection and Analysis. Brooks/Cole; 2001.
[50] Dry ME. The Fischer-Tropsch Process: 1950–2000. Catal Today 2002;71(3–4):227–41.